Chaos, Solitons and Fractals 178 (2024) 114328

Contents lists available at ScienceDirect

Chaos, Solitons and Fractals

journal homepage: www.elsevier.com/locate/chaos

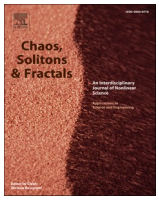

Quantifying the underlying landscape, entropy production and biological path of the cell fate decision between apoptosis and pyroptosis

Jun Jin [a], Fei Xu [b], Zhilong Liu [a], Jianwei Shuai [a,c], Xiang Li [a,*]

[a] Department of Physics, Xiamen University, Xiamen, Fujian 361005, China
[b] Department of Physics, Anhui Normal University, Wuhu, Anhui 241002, China
[c] Oujiang Laboratory (Zhejiang Lab for Regenerative Medicine, Vision and Brain Health) and Wenzhou Institute, University of Chinese Academy of Sciences, Wenzhou, Zhejiang 325001, China

ARTICLE INFO

Keywords:
Bifurcation analysis
Potential landscape
Shannon entropy
Dominant kinetic path
Cell death

ABSTRACT

Pyroptosis, a recently identified type of cell death, and apoptosis are fundamental and complex biological processes that underlie a multitude of diseases. However, the crosstalk between pyroptosis and apoptosis, as well as their molecular regulatory mechanisms governing decision-making, remain to be fully elucidated. In particular, comprehending how internal driving forces, including vital components of life such as proteins and reactions, collaborate with the environment to dictate cell fate remains an ongoing challenge. To address these issues, a cell death decision module model of the crosstalk between pyroptosis and apoptosis was developed. Stability analysis revealed the presence of three steady-state attractors within the death decision system: the apoptosis state attractor, the pyroptosis state attractor, and the concurrence state attractor. Landscape theory was employed to study the stochastic dynamic and global stability of the death decision system, allowing us to quantitatively describe the uncertainty of cell death decisions by measuring the production of Shannon entropy. In addition, we identified the dominant kinetic paths among different death mode attractors. We found that the dominant kinetic paths between different cell death modes usually do not pass through the minimum potential point. Through quantifying the underlying driving force of the system's dynamics, we determined that this phenomenon is attributed to the dependence of the driving force in non-equilibrium systems on both the gradient force and the curl force. In summary, this study offers a natural and physical groundwork for understanding the crosstalk network between pyroptosis and apoptosis, providing valuable insights and therapeutic strategies for the regulation of cell death modes in mammals.

1. Introduction

Cell death is one of the most fundamental events in the life of an organism, playing a crucial role in numerous essential biological processes. These processes include the elimination of useless, redundant and diseased cells, the maintenance of normal development, tissue morphology and organismal homeostasis, as well as the defense against pathogen invasion [1]. Excessive cell death can lead to the destruction of tissues, the immune system, and the nervous system, potentially resulting in diseases like AIDS, Alzheimer's disease, and Parkinson's disease. Conversely, inadequate cell death can lead to uncontrolled cell growth, causing malignant tumors, viral infections, and a wide range of other related diseases [2,3]. In response to changes in their own internal state and surrounding environment, cells possess the ability to undergo death actively or passively by starting different intracellular signal pathways [4]. Over the past three decades, the study of cell death has been a hot research field in life science [5], among which apoptosis and pyroptosis are the two most widely studied modes of cell death in recent years [4]. Only after a thorough understanding of the molecular mechanism of cell death, could we carry out drug intervention or even gene regulation on the proteins in the signal pathway to alleviate or cure these diseases.

After GSDMD was identified as the executor of pyroptosis in 2015 [6–8], pyroptosis has been gradually recognized as a very important programmed cell death mode. Pyroptosis causes massive release of cellular contents and induces inflammation. Many recent clinical studies show that people infected with COVID-19 are highly correlated with pyroptotic death signaling and inflammasomes [9–12]. Over the years,

* Corresponding author.
E-mail address: xianglibp@xmu.edu.cn (X. Li).

https://doi.org/10.1016/j.chaos.2023.114328
Received 15 October 2023; Received in revised form 25 November 2023; Accepted 28 November 2023

some molecular drugs such as resveratrol and disulfiram have been developed in clinical trials of COVID-19 treatment to control pyroptotic cell death by inhibiting inflammasome assembly and modifying GSDMD to prevent pore formation [11,13,14]. Unlike pyroptosis, apoptosis does not induce an inflammatory response during the elimination of excess cells in the body, thereby avoiding the risk of over-immunity [15,16]. However, numerous experiments have reported the close relationships between pyroptosis and apoptosis. High levels of GSDMD expression can rapidly induce pyroptosis [17]. When GSDMD is deficiency, activation of caspase-1 initiates apoptosis in cells [18]. Zheng et al. observed that GSDMD can disrupt mitochondrial membranes, leading to the release of cytochrome C and subsequent induction of apoptotic cell death [19]. Zhang et al. and Li et al. recently showed that inflammasomes can induce not only pyroptosis but also apoptosis [20,21]. Singh et al. found that SARS-CoV-2 infection can result in the activation of apoptosis as well as pyroptosis [11]. Although great achievements have been made in the study of switching strategies of cell fates, fundamental questions regarding how crosstalk pathways generate specific cell fate and what their potential mechanisms of switching are, remain unclear.

In the case of general dynamical systems, fluctuations are inevitable and they often need the exchange of energy, material and information with surrounding environment to maintain its stability [22]. Consequently, it becomes essential to investigate nonequilibrium dynamics to comprehend the fundamental principles and mechanisms. While the weight of the state can be quantified by potential landscape, the dynamics of the system are influenced by both the landscape and the flux. The landscape plays a role in stabilizing the system towards states or basins of attraction with higher probability or lower potential, while the flux introduces an additional force based on the net flow into or out of a particular state. To quantify the speed and manner in which the dynamics process occurs, a path integral formulation was previously developed [23]. Furthermore, one can quantify the dominant kinetic paths from one state to another. Due to the rotational nature of the flux force, the nonequilibrium transition states will be shifted away from the saddle point of the landscape. The kinetic rate is then determined by the effective barrier or action between the starting state and the nonequilibrium transition state. In addition to non-equilibrium dynamics, non-equilibrium thermodynamics can also be used to describe the natures of global emergence [24–26]. In fact, the thermodynamic cost for maintaining the function of the dynamical system can be quantified by the entropy production rate. From its definition, one can see that it is directly related to the rotational flux which is the nonequilibrium driving force [22]. Together with concepts and tools developed in other areas of nonequilibrium physics, significant progress has been made in unraveling the principles underlying efficient energy transport in cell cycle [27], as well as cell differentiation and development [28,29], aging [30], cancer [31–33], immune responses [33], neural networks and function of the brain [34], population dynamics and ecology [35], and evolution [36,37]. Here, we intend to explore how these theories work in the crosstalk between pyroptosis and apoptosis, which will provide a holistic view and physical explanation for the mechanistic understanding of death modes selection, offering potential therapeutic strategies for controlling various modes of cell death.

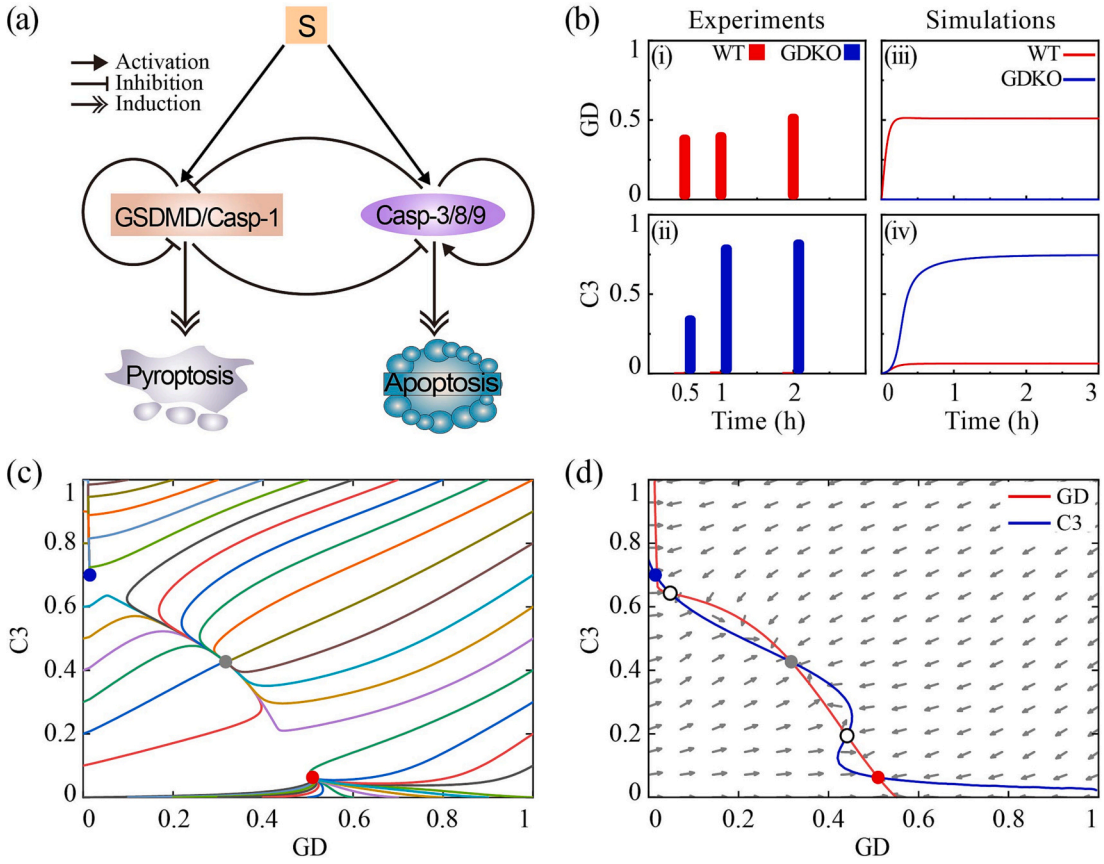

Fig. 1. Modeling the death decision module between pyroptosis and apoptosis. (a) The coarse-grained cell death decision module. The network contains pyroptosis constituent caspase-1/GSDMD and apoptosis constituent caspase-8/9/3. (b) Comparison between experimental data (histograms) and simulation results (lines) of the effectors time-course responses. (c) The trajectories from 40 sets of initial conditions in the GD–C3 phase plane, in which every trajectory converges to one of the three stable steady states. (d) Red and blue curves indicate nullclines for GD and C3, respectively. The vector field is indicated by gray arrows. Filled and open circles denote stable and unstable steady states, respectively. The unit is arbitrary. (For interpretation of the references to colour in this figure legend, the reader is referred to the web version of this article.)

2. Methods and results

2.1. Cell death decision module between apoptosis and pyroptosis

To investigate the regulatory mechanisms governing specific cell fate decisions, a coarse-grained cell death decision module based on the recently reported crosstalk between pyroptosis and apoptosis was developed. As shown in Fig. 1a, the module comprises two constituents, i.e., pyroptosis effector caspase-1/GSDMD and apoptosis effector caspase-8/9/3. In the pyroptosis constituent, caspase-1 cleaves and activates GSDMD to ignite pyroptosis [8]. However, the N-terminal fragment of GSDMD can also directly inhibit caspase-1, providing an efficient negative feedback loop for GSDMD activation [38]. In the apoptosis constituent, caspase-8/9 cleave caspase-3 and the cleaved caspase-3 also activate caspase-8/9, providing an efficient self-activation of this module for apoptosis induction [39–41]. Apoptosis and pyroptosis compete with each other. The apoptosis effector caspase-3 can suppress pyroptosis by inhibiting its effector, GSDMD [42]. In addition, GSDMD can indirectly block apoptosis by strongly inhibiting the intermediate processes involved in the activation of caspase-3. This is supported by recent experiments showing that apoptosis can occur in GSDMD deficient cells [6–8]. In addition, GSDMD can also inhibit caspase-3 by limiting the activation of its activators caspase-8/9 [18].

Based on the death decision module shown in Fig. 1a, we constructed a corresponding model described by two coupled ordinary differential equations (ODEs) presented below:

$$\frac{dGD}{dt} = k_{S\_GD} S \frac{(GD_{\text{tot}} - GD)^{n_1}}{(GD_{\text{tot}} - GD)^{n_1} + {J_{S\_GD}}^{n_1}} - k_1 GD \frac{GD^{n_2}}{GD^{n_2} + {J_{GD}}^{n_2}} - k_2 C3 \frac{GD^{n_3}}{GD^{n_3} + {J_{C3\_GD}}^{n_3}} - k_{GD} GD, \tag{1}$$

$$\frac{dC3}{dt} = k_{S\_C3} S \frac{(C3_{\text{tot}} - C3)^{n_4}}{(C3_{\text{tot}} - C3)^{n_4} + {J_{S\_C3}}^{n_4}} - k_3 GD \frac{C3^{n_5}}{C3^{n_5} + {J_{GD\_C3}}^{n_5}} + k_4 C3 \frac{(C3_{\text{tot}} - C3)^{n_6}}{(C3_{\text{tot}} - C3)^{n_6} + {J_{C3}}^{n_6}} - k_{C3} C3. \tag{2}$$

GD and C3 respectively represent the activation levels of pyroptosis constituent and apoptosis constituent. The first term on the right-hand side of Eq. (1) represents the activation term of GD induced by stimulation *S*. The second term on the right-hand side of Eq. (1) corresponds to the self-inhibition of species GD. The last two terms on the right-hand side of Eq. (1) describe the negative feedback effect of C3 on GD and the degradation/inactivation of GD. Eq. (2) describes the dynamics of C3, where the first term describes the stimuli-induced activation of C3. The second term represents the negative feedback effect of GD on C3. While the last two terms represent the self-activation and the degradation/inactivation of C3, respectively. GDtot and C3tot are the total levels of GD and C3. To obtain reliable model parameters, simulation was carried out and compared with the corresponding experimental data under the conditions of wildtype (WT) and GSDMD knockout (GDKO) (Fig. 1b) in BMMs. For WT BMMs (red histograms and lines), GSDMD is activated upon stimulation, and then GSDMD is cleaved and rapidly accumulated (Fig. 1b (i)) to trigger pyroptosis, whereas the apoptosis effector caspase-3 remain at rather low levels because of the inhibition effect of GSDMD (Fig. 1b (ii)). For GSDMD knockout BMMs (blue histograms and lines), caspase-3 is indirectly activated by stimulation, resulting in a shift from pyroptosis to apoptosis in the cells. Compared with WT, GSDMD knockout induces a delayed response of the apoptosis constituents (Fig. 1b (iii) and (iv)), resulting in a slower cell death pattern.

Experimental analysis of cell morphology suggests that cells can exhibit the states of apoptosis, pyroptosis, or the concurrence of pyroptosis and apoptosis under certain conditions [21]. Multistability is a fascinating phenomenon that occurs in dynamic systems where, for a given set of parameters, the system can exist in different stable states. The particular stable state that the system settles into depends on the initial conditions of the system. To examine the stability of the death decision model, we assumed the 2D system starts from different initial values and numerically solve Eqs. (1) and (2). We chose 40 sets of different initial conditions in GD-C3 phase plane, and the results presented in Fig. 1c show that their trajectories converge towards one of the three stable steady states, i.e., apoptosis state characterized by low GD and high C3 (blue point), concurrence state of apoptosis and pyroptosis characterized by medium GD and C3 (gray point), and pyroptosis state characterized by high GSDMD and low caspase-3 (red point). To understand the dynamics of the 2D system graphically, we obtained the nullclines of GD and C3 by setting dGD/dt = 0 and dC3/dt = 0, and compute the vector field in the phase plane. As clearly depicted in Fig. 1d, the two nullclines intersect at five points, which represent two unstable steady states and three stable steady states, as the vector field indicates the system moves from any point towards one of the three stable states. Collectively, consistent with the experimental observations, our steady-state results on the phase plain reveal that the apoptosis and pyroptosis death decision system exhibits tristability.

2.2. Global stability analysis reveals the multi-death modes determined by stimulus

We next employed bifurcation analysis to assess the expression level of protein and reactions that can induce the switch between different death modes in this section. We first took stimulus intensity (S) as the bifurcation parameter to investigate its effects on the effector proteins, i.e., C3 and GD. The corresponding bifurcation diagram is plotted in Fig. 2a. With the increase of stimulus intensity S, the system will go through five phases (phase I, II, III, IV, and V) with different numbers of stable states. In phase I (light blue region), the stimulus intensity S is small ($< \sim 0.33$) and the system exists a single stable state. The activated GD is stable at a low value (top panel in Fig. 2a), while the level of activated C3 is high (bottom panel in Fig. 2a). The timeseries of an illustrative example (point 1) when S = 0.2 in Fig. 2b indicate that cells will die only in the form of apoptosis. With the increase of stimulus intensity S (phase II enclosed by saddle node bifurcation points SN1 and SN2), the system exhibits bistability, i.e., two stable steady state (solid lines) separated by an unstable steady state (dashed line). SN1 is the low threshold of stimulus intensity S (~ 0.33) for GD activation and C3 inactivation, while SN2 is the high threshold (~ 0.53) for GD inactivation and C3 activation. In the bistable region, which steady state the system will reach mainly depends on the initial conditions. Small perturbations of the initial condition may lead to different cell death modes. For example, at S = 0.4, the system finally evolves to a stable state with a high level of GD and a low level of C3 (Fig. 2b, point 2) from initial values of (0.5, 0.16), resulting in pyroptosis. If we drive the initial activation level of C3 from 0.16 to 0.17, the timeseries will converge to a low GD and high C3 steady-state values (Fig. 2b, point 3), resulting in apoptosis.

As the stimulus intensity S gradually increases from 0.53 to 0.63 (phase III, light yellow region), a new stable steady state with both high level of GD and C3 (Fig. 2b, point 4) is observed compared with region II, indicating the concurrence of apoptosis and pyroptosis. As the stimulus is further increased to orange region of phase IV ($0.63 < S < 0.85$), the steady-state representing apoptosis annihilate. When the stimulus intensity S is large enough ($> \sim 0.85$), the system exhibits a stable state and the activated GD maintains at a high level, which gradually increases with the increase of stimulus intensity (phase V, light pink region), while C3 is stable at a quite low level, occurring pyroptosis only. Bifurcation analysis above suggest that the stimulus intensity S play a crucial role in determining the mode of cell death, whether it be apoptosis, pyroptosis or a concurrence of both. These results are supported by our previous observed experimental data in RAW-asc cells upon lethal toxin (LT) stimulation [21]. As shown in Fig. 2c, occurrences of pyroptosis and apoptosis were measured by the release of lactate

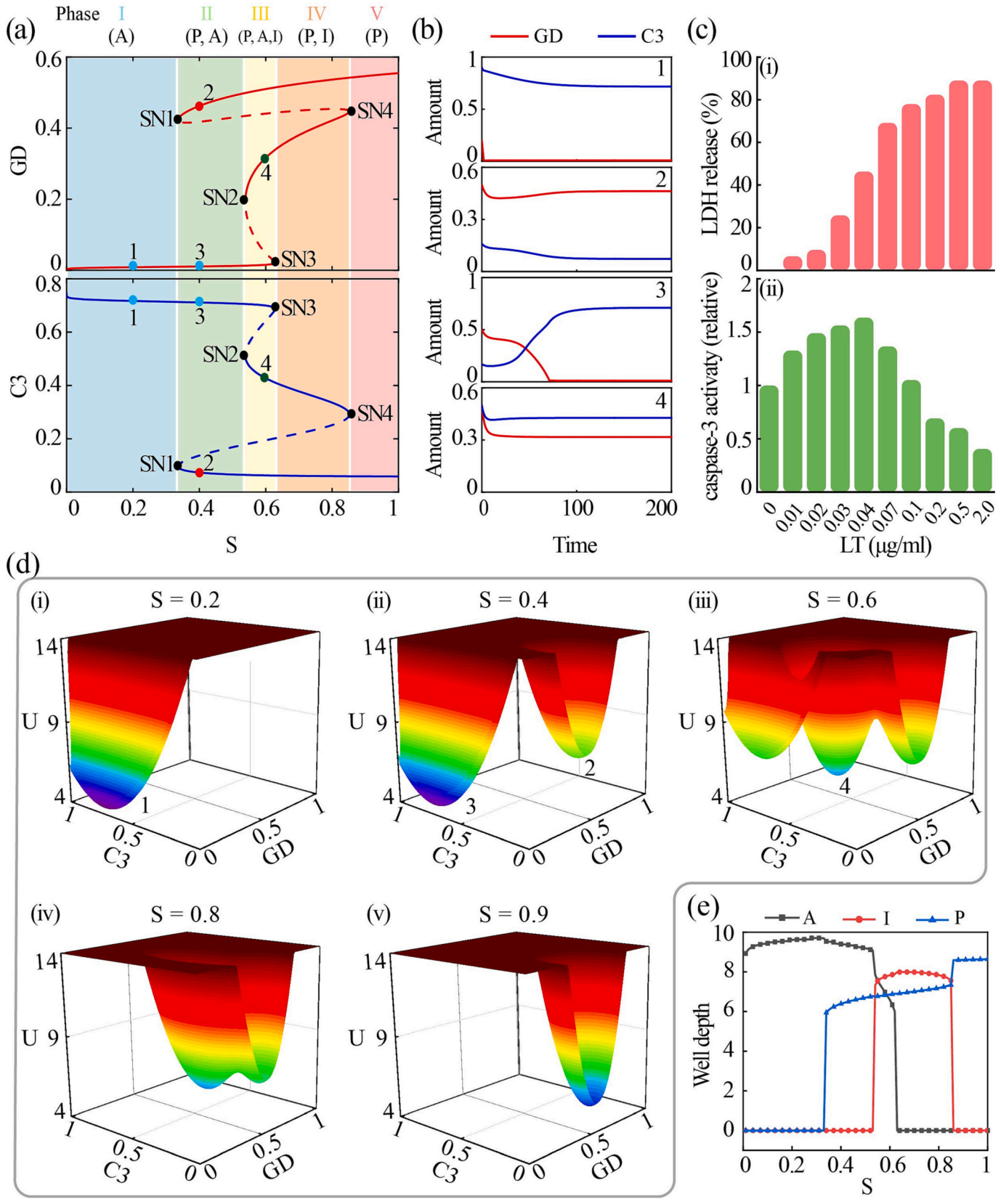

Fig. 2. Bifurcation diagram and global stability of the death decision system. (a) Bifurcation diagram of GD and C3 as a function of stimulus intensity S. Solid lines indicate stable steady states, and dashed lines indicate unstable steady states. According to the number of steady states, the diagram can be divided into five phases. (b) Time series of GD and C3 corresponding to points 1, 2, 3 and 4 in fig. (a), respectively. (c) LDH release and caspase-3 activity with LT concentration increases. (d) Potential landscape changes when stimulus intensity (S) is 0.2 (i), 0.4 (ii), 0.6 (iii), 0.8 (iv), 0.9 (v), respectively. (e) The well depth of apoptosis, pyroptosis and co-occurrence state change as stimulus intensity changes. A, apoptosis state; P, pyroptosis state; I, concurrence state of apoptosis and pyroptosis.

dehydrogenase (LDH) and relative activity of caspase-3. With increasing LT concentration, the release of LDH increases gradually (Fig. 2c (i)), while caspase-3 activity exhibits a gradual increase followed by a subsequent decrease (Fig. 2c (ii)). This means that cells will only die in the form of apoptosis with low dose of LT. With the increase of LT concentration, cells will die of apoptosis, pyroptosis, or the concurrence of apoptosis and pyroptosis.

The mode of cell death is influenced by intrinsic or external fluctuations [43,44]. In order to comprehensively investigate the stochastic properties of the death decision system, the generalized potential landscape [26,45] was used to characterize the system's dynamic behavior in phase space from a global perspective. The stochastic dynamics can be described by Langevin equation, i.e., $dC_i(t)/dt = F_i(C) + \eta_i(t)$, where C_i represents the concentration of species. $F_i(C)$ represents the driving force that describing the dynamics of the system. The term $\eta_i(t)$ represents fluctuation or noise force, which obeys Gaussian distribution with correlation function $<\eta_i(t)\,\eta_j(t')> = 2D_{ij}\,\delta_{ij}\,\delta(t-t')$, where δ_{ij} is the Dirac delta function, and D is the diffusion coefficient matrix characterizing the strength of the fluctuations. Here, we assumed the isotropic and homogeneous case $D_{11} = D_{22}$. The probability evolution P for the system can be reflected by Fokker-Planck equation:

$$\frac{\partial P(C,t)}{\partial t} = -\sum_i \frac{\partial}{\partial C_i}[F_i(C)P(C,t)] + \sum_i D_i \frac{\partial^2}{\partial {C_i}^2} P(C,t) \tag{3}$$

The global steady-state probability distribution P_{ss} of the state space can be obtained by solving the steady-state solution of above Fokker-Planck equation. The corresponding dimensionless potential U can be calculated by the Boltzmann relation, $U = -\log(P_{ss})$. Since the computational efficiency limits the direct access to the probability density through the evolution of the Fokker–Planck equation. We used the self-consistent mean field approximation method [46] to replace the steady-state probability distribution.

The effects of stimulus intensity (S) on the global stability of the system was investigated and the corresponding potential landscapes on GD-C3 phase panel are shown in Fig. 2d. The basin with lower potential or higher probability represents a mode of cell death. When S = 0.2, the system exhibits a monostable landscape, implying that cells will die only in the form of apoptosis no matter what initial levels of the constituent are (Fig. 2d (i)). However, with a relative high stimulus intensity (S = 0.4), the landscape exhibits two basins of attraction, which characterizes apoptosis state and pyroptosis state (Fig. 2d (ii)). Noise can drive cells to switch between these two death modes, but cells tend to stay in apoptosis state due to lower potential. As the stimulus intensity further increases to 0.6 (Fig. 2d (iii)), a new basin representing coexistent state of apoptosis and pyroptosis is observed. The relative stability of the three stable states is correlated to the depth of potential valley. As S increases further (S = 0.8), the apoptosis state becomes less stable and finally disappears (Fig. 2d (iv)). Finally, the system evolves to a single pyroptosis landscape at S = 0.9 (Fig. 2d (v)). To quantify the landscape topology, we measured the well depth, the difference between basin and maximum potential surface. As the results shown in Fig. 2e, too small ($< \sim 0.33$) or too large ($> \sim 0.85$) intensity of S respectively induces the sole occurrence of apoptosis or pyroptosis. The depth of the apoptosis basin is decreased with the increase of S (black line), while the depth of pyroptosis basin is increased (blue line). The basin representing coexistent state of apoptosis and pyroptosis appears with the deepest in the region of $0.53 < S < 0.85$, indicating cells tend to die in the form of co-occurrence. Compared to bifurcation analysis, potential landscape analysis enables not only the observation of multistability, but also the accurate description of the transition dynamics of the system by quantitatively calculating the potential of each basin. The application of potential landscape analysis provides a more convenient approach to understand the stochastic dynamics and global stability of the death decision system.

2.3. Shannon entropy quantifies the uncertainty of multi death modes

In cell death decision system, the dynamics of multi death modes can be observed at appropriate stimulus intensity, as the two or three basins shown in Fig. 2d. To measure the switching ability of the system among different states, Shannon entropy (*SE*), defined as $SE = -\sum_i p_i log_2 p_i$, was used to quantify the uncertainty of cellular fate decisions [47]. p_i represents the probability of different death modes. When $SE = 0$, the system presents a single ordered state. The larger the value of *SE* is, the more disordered the system is. The produce for calculating *SE* shown in Fig. 3a. Firstly, the time series of variables was recorded by running the corresponding Langevin equation of the deterministic system with random initial state. Here we selected C3 because of its identifiability in cell death modes. Then the relative frequency of C3 was fitted with mixed Gaussian function. Finally, we used the normalized area under each peak of mixed Gaussian function as the probability of corresponding death mode to further calculate *SE*. As shown in Fig. 3b, the generated frequency distributions of C3 vary with stimulus intensities.

The quantified Shannon entropy of the expression level of C3 and GD in regulating coexistent dynamics are shown in Fig. 3c, revealing that highly disordered states are more easily observed in the high level regions of C3 and GD. The colour region other than blue is the coexistence transition region and the colour codes indicate the degree of transition among different death modes. The red region presents a highly disordered state and high entropy production of the system. With further increase of GDtot and C3tot, *SE* gradually decreases, and apoptosis and pyroptosis becomes dominated. A more intuitive landscape topography transition is shown in Fig. 3d when GDtot is fixed at the value of 1.3. When C3tot = 0.5, the system presents a highly ordered state, i.e., only a pyroptosis basin (Fig. 3d (i)). As C3tot increases to 1.05 and 1.12, the cell fate switches from ordered pyroptosis to disordered state among different cell death modes (Fig. 3d (ii) and (iii)). With further increase of C3tot, the depth of apoptosis basin gradually exceeds that of pyroptosis basin, suggesting that C3tot biases the cell fate towards apoptosis (Fig. 3d (iv)). The transitions of Shannon entropy and potential landscape topography with different GDtot are also investigated with C3tot is fixed at 1.1 (Fig. 3e). In contrast to C3tot, increase of GDtot results in the uncertainty of cell fate switches from ordered apoptosis to highly disordered state, giving the depth of apoptosis basin decreased and pyroptosis basin increased. This result is qualitatively supported by the experimental observations that pyroptosis occurs in cells with a high GSDMD expression level, such as macrophage and the small intestine in mice, while apoptosis occurs in cells with a low GSDMD expression level, for example, spinal cord and L929 cells [18].

Therefore, C3 and GD expression levels also can act as the driving forces to selectively control the mode of cell death. The system exclusively executes apoptosis at low GD level and pyroptosis at low C3 level. Increase of C3 and GD significantly elevates entropy production. The death decision system is highly disordered and will selectively undergo different death modes, depending on the expression conditions. Coexistent dynamics regulated by stimulus intensity S and the expression level of C3 or GD are shown in Fig. S1, indicating that we can selectively control the mode of cell death by adjusting the stimulation intensity and the level of C3 or GD.

2.4. Quantifying the dominant kinetic paths among different death modes

In above section, we utilized Shannon entropy to quantify the uncertainty of coexistence death mode, and the greater Shannon entropy, the more frequent the system switches among attractors. Based on large deviation theory, transition path theories were used to quantify the most probable path for the transition between attractors [48,49]. To further reflect the dynamical process of transition from one attractor to another, we resorted to path-integral approach [46,50] to minimize the transition actions and obtain the most probable switching path, known as

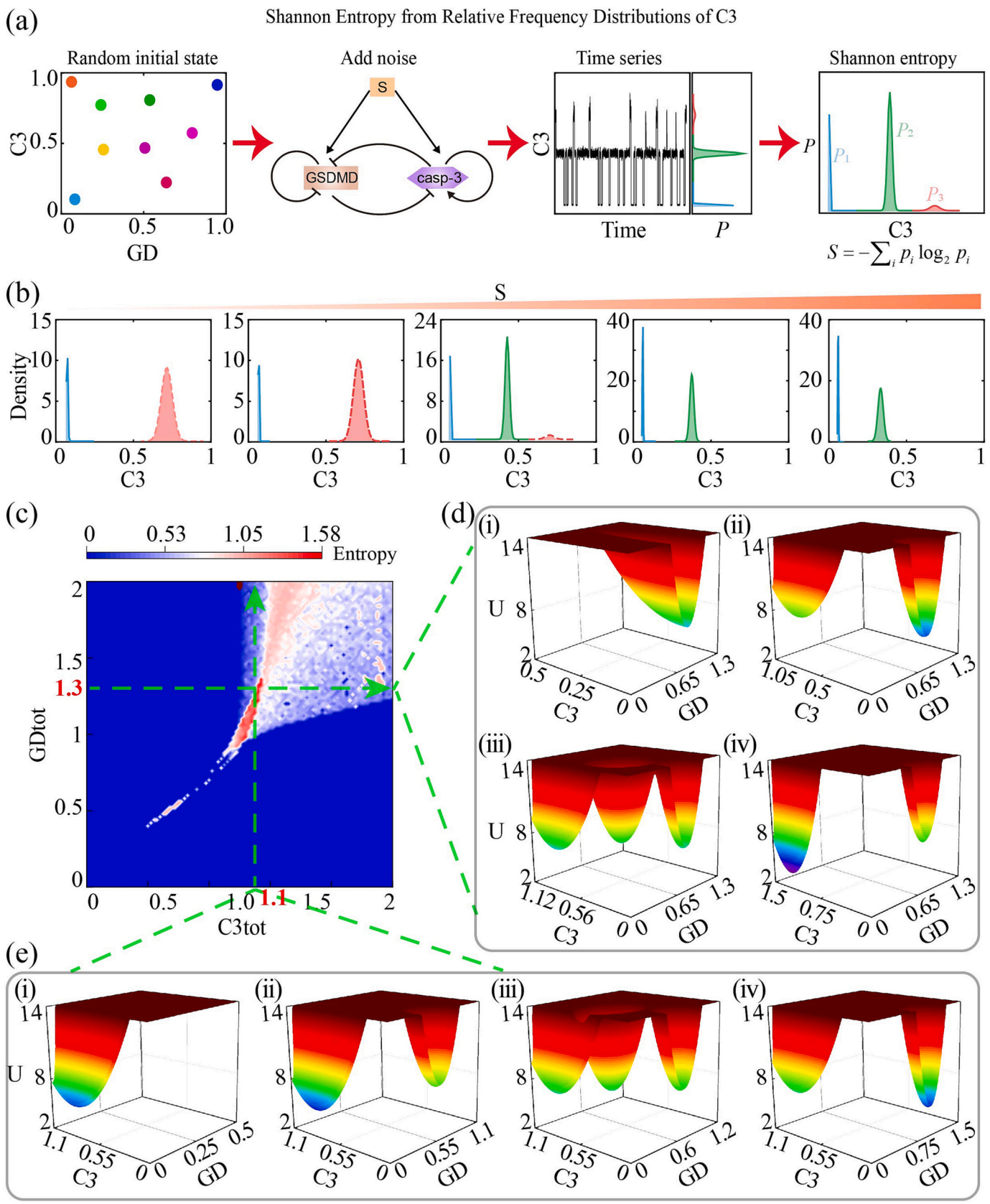

Fig. 3. Shannon entropy quantifies the uncertainty of cell fate decisions. (a) Illustration of the calculation procedure of Shannon entropy. (b) Statistics and distribution of C3 under five representative stimulus intensity. (c) The quantified Shannon entropy of coexistent dynamics in GDtot-C3tot phase plane. (d) and (e) The potential landscape topography of death modes with GDtot = 1.3, and C3tot at 0.5, 1.05, 1.12, and 1.5 respectively (d), and the level of C3tot at 1.1 with GDtot = 0.5, 1.1, 1.2, and 1.5 respectively (e).

dominant kinetic path.

Based on the path-integral approach [46,50], we have

$$P_t\left(\mathrm{x}_{\mathrm{final}}, t, \mathrm{x}_{\mathrm{initial}}, 0\right) = \int D\mathrm{x} exp\left[-\int dt\left(\frac{1}{2}\nabla\cdot\mathrm{F}(\mathrm{x}) + \frac{1}{4}\left(\frac{dx}{dt} - \mathrm{F}(\mathrm{x})\right)\cdot\frac{1}{D(\mathrm{x})}\cdot\left(\frac{dx}{dt} - \mathrm{F}(\mathrm{x})\right)\right)\right] = \int D\mathrm{x} exp[-S(\mathrm{x})] = \int D\mathrm{x} exp\left[-\int L(\mathrm{x}(t))dt\right], \tag{4}$$

where P_t represents the transition probability, $S(\mathrm{x}(t))$ is the action, and $L(\mathrm{x}(t))$ is the Lagrangian. To calculate the most probable transition path from one stable state to another one, we need to minimize the action S to maximize the transition probability. Here, the Lagrangian is written as

$$L(\mathrm{x}) = \frac{1}{4D}\dot{\mathrm{x}}^2 + V(\mathrm{x}) - \frac{1}{2D}F(\mathrm{x})\cdot\dot{\mathrm{x}}, \tag{5}$$

where $V(X) = \frac{1}{4D}\mathrm{F}^2 + \frac{1}{2}\nabla\cdot\mathrm{F}(\mathrm{x})$. So, we can write the generalized momentum and Hamiltonian

$$Pm(\mathrm{x}) = \frac{\partial L}{\partial\dot{\mathrm{x}}} = \frac{1}{2D}(\dot{\mathrm{x}} - \mathrm{F}(\mathrm{x})), \tag{6}$$

and

$$H(\mathrm{x}) = -L(\mathrm{x}) + P_m(\mathrm{x}).\dot{\mathrm{x}} = E_{eff}. \tag{7}$$

Here, we chose $E_{eff} = -V_{\min}$, with $V_{\min}$ being the minimum of effective potential. In this case, the path connects two stable states, so V will reach its minimum when x is the most stable state among multiple stable states.

Then, we substituted Eq. (7) into the action and obtain $S(\mathrm{x}) = \int(P_m(\mathrm{x}).\dot{\mathrm{x}} - H(\mathrm{x}))dt$. To calculate the action of the path, we need to transform the formulations into a different representation in x space and discretize the integral. The target function can be written as

$$S = \sum_{n=1}^{N-1}\left(\sqrt{(E_{eff} + V(n))/D} - \frac{1}{2D}F_l(n)\right)\Delta l_{n,n+1} + \lambda P, \tag{8}$$

where N is the total number of points on the transition path and P is a penalty function keeping all the length elements close to their average, where

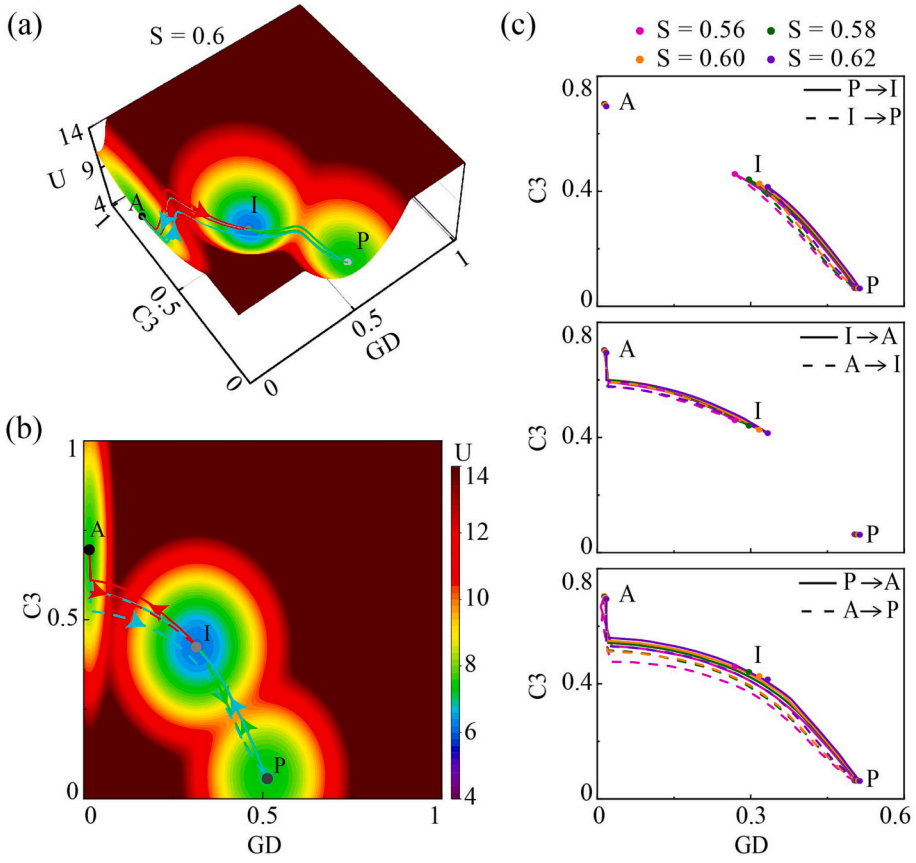

Fig. 4. The dominant kinetic paths between different attractors. The landscape and kinetic paths in the GD-C3 plane shown in three-dimensional (a) and two dimensional (b) figures. The cyan curves denote the dominant kinetic paths between A state and P state, the red lines denote the dominant kinetic paths between A state and I state, and the green lines denote the dominant kinetic paths between P state and I state. (c) Influence of stimulus intensity S on the dominant kinetic paths. A, apoptosis state; P, pyroptosis state; I, concurrence state of apoptosis and pyroptosis. (For interpretation of the references to colour in this figure legend, the reader is referred to the web version of this article.)

$$P = \sum_{n=1}^{N-1} \left(\Delta l_{n,n+1} - \langle \Delta l \rangle\right)^2,$$

and

$$(\Delta l)^2_{n,n+1} = \sum_i (\mathrm{x}_i(n+1) - \mathrm{x}_i(n))^2,$$

$$F_l(n) = \sum_i \mathrm{F}_i(\mathrm{x}(n))(\mathrm{x}_i(n+1) - \mathrm{x}_i(n)) \Big/ \Delta l_{n,n+1},$$

$$V(n) = \sum_i \left(\frac{1}{4D}\mathrm{F}^2(\mathrm{x}_i) + \frac{1}{2}\sum_j \frac{\partial \mathrm{F}_j(\mathrm{x}_i)}{\partial x_j}\right),$$

where N represents the number of components (here $N = 2$) and i is the index for different dimensions. In this way, we can calculate the transition action of any path. Finally, we can obtain the dominant kinetic path by minimizing the transition action S.

We calculated the dominant kinetic path between neighboring stable states under standard parameters. The dominant kinetic paths are shown on the potential landscape in Fig. 4a, wherein Fig. 4b is a vertical view of the three-dimensional potential landscape of Fig. 4a. Three distinct basins emerged on the potential landscape, characterizing three stable cell states including apoptosis (A), pyroptosis (P), and concurrence of apoptosis and pyroptosis (I) according to the death decision system. The lines connecting two different stable states represent the dominant kinetic paths, and the arrows indicate the directions of the transition. It is notable that the forward and backward dominant kinetic paths are irreversible. The dominant kinetic paths between pyroptosis state (P) and concurrence state (I) (green lines) tends to pass through the saddle, while the dominant kinetic paths between A state and P state (cyan lines), A state and I state (red lines) are not. We further explored the influence of stimulus intensity S on the dominant kinetic paths (Fig. 4c). It is suggested that the position of I state changed obviously, while the A state and P state changed only slightly. With the increase of S, the dominant kinetic paths between I state and P state shift to the right (top panel in Fig. 4c), while the dominant kinetic paths between A state and P state shift upward (bottom panel in Fig. 4c). Among them, the dominant kinetic path from A state to P state changes more obviously than that from P state to A state. Compared with these dominant kinetic paths, the dominant kinetic paths between A state and I state have negligible variations (middle panel in Fig. 4c).

We next tried to investigate the underlying mechanism responsible for the differences of dominant kinetic paths among cell fate. As shown in Fig. 5a, the green solid and dotted lines represent the dominant kinetic paths from P state to I state and from I state to P state, respectively, where the maximum potential points in the dominant kinetic paths are indicated by magenta dots. Connecting these two maximum potential points will result in a ridge (blue line in Fig. 5a) that separates the two valleys, P and I. It can be clearly seen from the potential curve corresponding to the ridge that the dominant kinetic paths pass through its minimum potential point (Fig. 5b). Further, we selected a series of blue

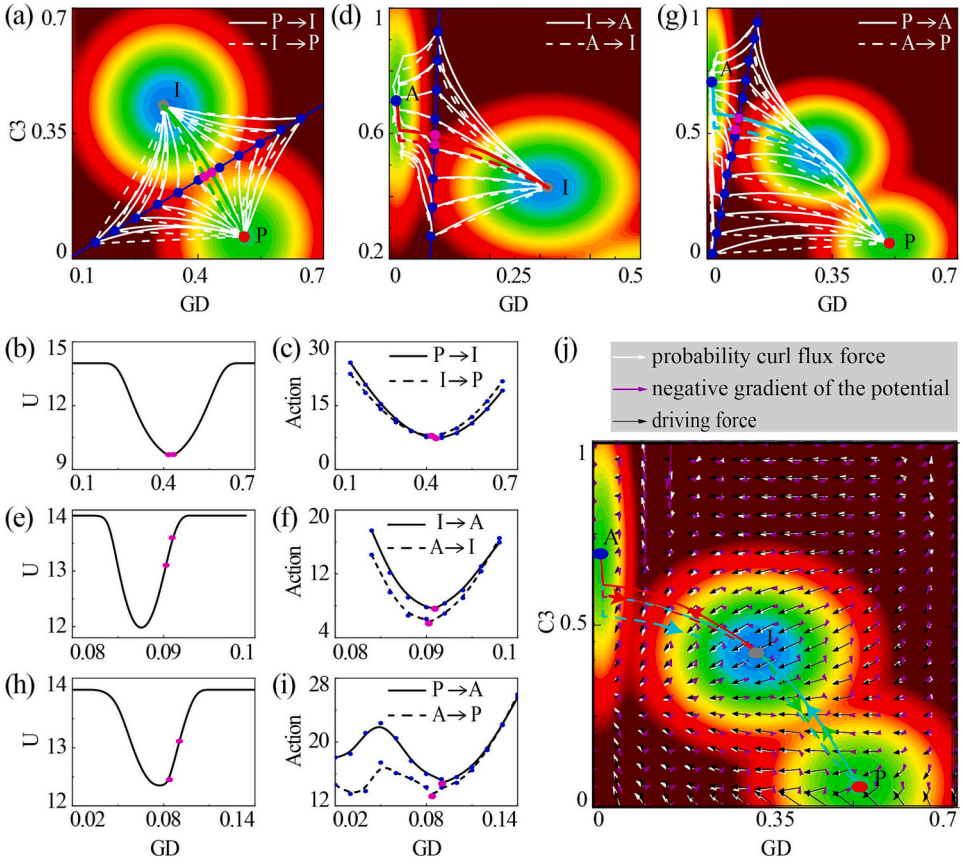

Fig. 5. Mechanism analysis of the dominant kinetic paths among apoptosis state (A), pyroptosis state (P), and concurrence state of apoptosis and pyroptosis (I). Dominant kinetic paths between P state and I state are represented by green lines in (a), between I state and A state by red lines in (d), and between P state and A state by cyan lines in (g). The maximum potential points in the dominant kinetic paths are indicated by magenta dots. Blue lines represent the corresponding ridges. White lines are the dominant kinetic paths restricted to passing through the blue points in the ridges. (b), (e) and (h) are the potential curves of the corresponding ridges in (a), (d) and (g), respectively. (c), (f) and (i) are the action curves of the dominant kinetic paths passing through the ridge in (a), (d) and (g), respectively. (j) Illustration of dominant kinetic path and flux among three basins of attraction in death decision system. (For interpretation of the references to colour in this figure legend, the reader is referred to the web version of this article.)

points along the ridge and calculate the dominant kinetic paths passing through these points. The dominant kinetic paths from P state to I state and from I state to P state are represented by white solid lines and dotted lines, respectively, in Fig. 5a. The action of these dominant kinetic paths is displayed in Fig. 5c, where the horizontal ordinate indicates the dominant kinetic path passing through the point with the same GD in the ridge line in Fig. 5a. These outcomes also confirmed that the dominant kinetic paths (green lines in Fig. 5a) between P state and I state have the smallest action (magenta dots in Fig. 5c).

Unexpectedly, further analysis of the dominant kinetic paths between I state and A state (Fig. 5d) and between P state and A state (Fig. 5g) shows that they do not pass through the minimum potential point (Fig. 5e and h), but their action is also the smallest (Fig. 5f and i). To address this issue, we quantified the steady-state probability flux of the cellular fate decisions landscape in Fig. 5j. The driving force, represented by black arrows, in this non-equilibrium system is decomposed into steady-state probability flux and the negative gradient of the potential landscape, which are represented by white and purple arrows, respectively. The direction of the arrow and the length of the line segment indicate the direction and magnitude of the force respectively. These results indicated that the dynamics of cell-fate decisions network are not only determined by the gradient of the underlying landscape but also by the curl force from the non-equilibrium current flux [24,50,51]. As can be seen from Fig. 5j, the curl force from the steady-state probability flux plays a leading role in most region, resulting the dominant kinetic paths to deviate from the conventionally expected potential gradient paths. Although the forward and backward dominant kinetic paths are irreversible, implying the irreversiblility of selection process of cells between two different fates, each of them follows the principle of minimum action.

Mean first-passage time (MFPT) was widely employed to quantify the average escape time of the alternations from one attractor to another, describing the stability of attractors [52,53]. With stochastic dynamical trajectories spanning a lengthy time window, we can estimate the time required for the cell death decision module model to transition from one attractor to another for the first time and obtain the first passage time (FPT). In this context, an attractor region is approximately defined as a small ellipse centered on the local minimum, and the transition is considered complete once the stochastic trajectory enters the target ellipse [54]. Subsequently, MFPT is defined as the average of FPT by samplings. Fig. 6 shows the MFPT between different death attractors induced by different intensities of noise under standard parameters. We can see that all the MFPTs between different cell death attractors are decreased with the increasing of noise intensity (D). It is consistent with our cognition that greater noise intensity can lead to greater instability in the steady state, and noise will make it easier for cells to escape from the steady state. Although all MFPTs decrease with the increasing noise intensity, the MFPT from A state to I state (black line) is the smallest, suggesting that cells prefer to exist in I state compared to A state.

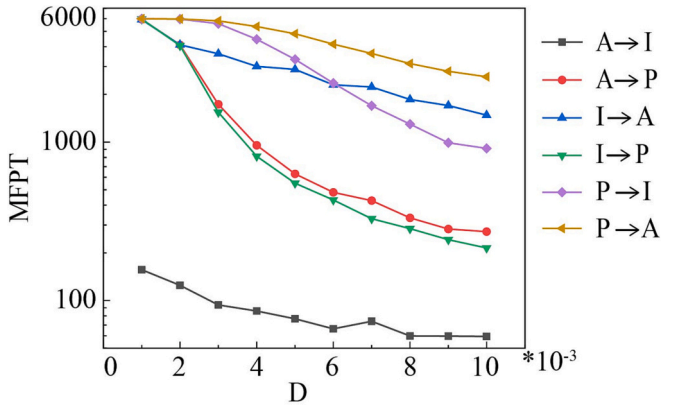

Fig. 6. The MFPTs between different cell death attractors with the increase of noise intensity. A, apoptosis state; P, pyroptosis state; I, concurrence state of apoptosis and pyroptosis.

3. Discussion

Cellular death is a fundamental and complex biological process that is an underlying driver for many diseases [2,3]. Although extensive studies have focused on understanding the molecular mechanisms of various forms of cell death, emerging evidence suggests intricate crosstalk among different cell death pathways [38,55]. To dissect how different pathways collaborate to determine specific cell fate within the crosstalk network of apoptosis and pyroptosis, we developed a coarse-grained cell fate decision model based on recent experimental findings and data in this study. Stability analysis, bifurcation analysis, landscape theory, and Shannon entropy were employed to systematically quantify how each component and reaction within the crosstalk network contribute to the transitions between different death modes. Furthermore, we utilized path integral theory to describe the most probable transition paths and their feasibility among different death modes.

The state of a cell that performs a certain function corresponds to the attractor of a dynamic system. Stability analysis indicates that there are three attractors, i.e., three different cell fates in our model and we can adjust the different cell fates through the initial expression levels of GD and C3. Nevertheless, stability analysis can only reveal the final fate of cells. While with bifurcation analysis, we further manifest that both constituents and reactions in the death decision system can efficiently induce multi-death modes (Fig. S2). A single-parameter bifurcation analysis discusses the system's stable state with all other parameters at standard values, whereas the phase diagram can illustrate the synergistic modulation of two parameters on the number of stable states. We explored the distribution of stable states concerning any two of the reaction parameters (Fig. S3). Specifically, the distribution concerning k_{S_GD} and k_{S_C3} reveals that the number of stable states can undergo three-state switching (from monostability to bistability, back to monostability) (Fig. S3a, blue line), and five-state switching (from monostability to bistability, then to tristability, back to bistability, and finally to monostability) (Fig. S3a, red line), with an increase in k_{S_GD}, depending on the value of k_{S_C3}. Similar results of state distribution are observed in other phase diagrams containing the parameter k_{S_GD} (Fig. S3a-g), indicating the intricate role of k_{S_GD} in mediating diverse transitions of stable states. Moreover, in most phase diagrams involving parameter k_{C3}, it is observed that the parameter space for multistability is relatively small (Fig. S3g, r, v, y-aa), suggesting a limited role of k_{C3} in regulating the occurrence of multiple death modes. While the phase diagram with respect to k_1 and k_{S_C3} (Fig. S3ab) exhibits a large multistable space, enabling efficient modulation of the switch from tristability to bistability when k_1 is small. Compared with stability analysis and bifurcation analysis, potential landscape can intuitively provide global characterization and stability measurement to capture the dynamic principle of cell state transition. The application of potential landscape deepens our understanding of biological functions. However, it is still difficult to solve a high-dimensional Fokker-Planck equation to obtain the evolution probability because of the huge state space of the complex system. Thus, the self-consistent mean field approximation method is a good choice to solve the above problems [46].

Potential landscape transforms the study of complex systems, shifting the focus from following individual trajectories to tracking the evolution of system states [22]. The whole system can be characterized by the states with weights, which are determined by the depths of the underlying landscape. The different energy basins or valleys represent possible functional states of the protein and their importance is reflected by their associated weights [56–58]. For equilibrium systems, the energy landscape theory put forward a new viewpoint of protein folding: there are multiple pathways that guide the system towards the folded

state during the early stages. As the folding progresses, local traps become influential, offering distinct routes for the folding process. The introduction of biasing greatly accelerates the search for the native state, effectively resolving the protein folding paradox through the concept of a funnel landscape [59]. The statistical energy landscape approach gave a new way to define the specificity for binding, which is used to generate the optimized scoring function for reaching both high affinity and specificity for ligand binding, protein-RNA(DNA) binding, and protein–protein binding [60]. The new way has been successfully applied to the drug discovery for identifying the lead compounds with specificity against the targets [61–66]. The funneled landscape can also be used to predict the function and stability for protein binding and folding. It is probable that the evolutionary process has predominantly explored a limited portion of the state space available to folded and functional proteins. Consequently, a completely random search is unlikely. In addition to random mutations, the evolution and selection of proteins and their interactions are influenced by environmental constraints. These factors, in alignment with Darwin's theory of natural evolution based on the survival of the fittest, play a crucial role [67,68].

Coexistence dynamics in crosstalk networks with different death modes have also been widely explored. We previously investigated the coexistence dynamics between pyroptosis and secondary pyroptosis [69], pyroptosis and apoptosis [21,55], necroptosis and apoptosis [47,70], by constructing corresponding regulatory signaling networks. Compared with the previous work, we established a cell death decision module model of the crosstalk between pyroptosis and apoptosis, and well reproduced the experimental observations. In addition, the path integral theory was applied to the cell death model for the first time and the dominant kinetic transition paths among different death modes was successfully dissected. We found that the forward and backward dominant kinetic paths between two stable state are irreversible, and the dominant kinetic paths do not always pass through the saddle (Fig. 5). This is because the driving force of the non-equilibrium system is determined by the gradient of the underlying landscape and the curl force from the non-equilibrium current flux, which together determine the minimum action of the dominant kinetic path. At the same time, we also found that the transition between apoptosis and pyroptosis go through the coexistence state of apoptosis and pyroptosis and stay for a period of time (Fig. 4b), and then its final fate is determined according to the newly accumulated evidence, which provides us with ideas for regulating the fate of cells.

Our bifurcation analysis unveils the pivotal role of GD expression levels in triggering the switch between cell death modes, encompassing apoptosis or pyroptosis alone, as well as the concurrent occurrence of apoptosis and pyroptosis (Fig. S2). This is corroborated by previous experimental observations in RAW-asc cells, where the activities of GSDMD and caspase-1 can be detected, while the apoptotic transducers caspase-3 remain inactive, indicating that the cells undergo cell death in the form of pyroptosis [21]. Conversely, the activation of caspase-3 is detected in Gsdmd deletion cells, indicating a switch from pyroptosis to apoptosis. Microscopy experiments further underscore the pivotal role of GSDMD in switching cell death mode from pyroptosis to the concurrence of apoptosis and pyroptosis, and ultimately to apoptosis. However, as of now, there is no direct evidence supporting our other predictions, such as the dominant kinetic paths and escape time between these three death attractors. We anticipate that the new insights uncovered in this study can be substantiated through future experiments. Furthermore, we hope these findings will provide guidance for potential strategies and drug development related to diseases associated with apoptosis and pyroptosis.

CRediT authorship contribution statement

Jun Jin: Conceptualization, Formal analysis, Writing – original draft. **Fei Xu:** Data curation, Formal analysis. **Zhilong Liu:** Data curation, Validation. **Jianwei Shuai:** Funding acquisition, Writing – review & editing. **Xiang Li:** Conceptualization, Formal analysis, Funding acquisition, Writing – original draft.

Declaration of competing interest

The authors declare that they have no known competing financial interests or personal relationships that could have appeared to influence the work reported in this paper.

Data availability

The ODE model is developed and simulated with Python 3.8.2. Zipped mathematical code files of the model to generate the results in this study are available upon request from the corresponding author.

Acknowledgments

This work was supported by National Natural Science Foundation of China (Grant No. 12090052), Natural Science Foundation of Fujian Province of China (Grant No. 2023J05002), and the Fundamental Research Funds for the Central Universities (Grant No. 20720230017).

Appendix A. Supplementary data

Supplementary data to this article can be found online at https://doi.org/10.1016/j.chaos.2023.114328.

References

[1] Green DR, Levine B. To be or not to be? How selective autophagy and cell death govern cell fate. Cell 2014;157:65–75.
[2] Bredesen DE, Rao RV, Mehlen P. Cell death in the nervous system. Nature 2006;443:796–802.
[3] Galluzzi L, Buque A, Kepp O, Zitvogel L, Kroemer G. Immunogenic cell death in cancer and infectious disease. Nat Rev Immunol 2017;17:97–111.
[4] Bedoui S, Herold MJ, Strasser A. Emerging connectivity of programmed cell death pathways and its physiological implications. Nat Rev Mol Cell Biol 2020;21:678–95.
[5] Green DR. The coming decade of cell death research: five riddles. Cell 2019;177:1094–107.
[6] Shi J, Zhao Y, Wang K, Shi X, Wang Y, Huang H, et al. Cleavage of GSDMD by inflammatory caspases determines pyroptotic cell death. Nature 2015;526:660–5.
[7] Kayagaki N, Stowe IB, Lee BL, O'Rourke K, Anderson K, Warming S, et al. Caspase-11 cleaves gasdermin D for non-canonical inflammasome signalling. Nature 2015;526:666–71.
[8] He WT, Wan H, Hu L, Chen P, Wang X, Huang Z, et al. Gasdermin D is an executor of pyroptosis and required for interleukin-1β secretion. Cell Res 2015;25:1285–98.
[9] Yap JKY, Moriyama M, Iwasaki A. Inflammasomes and Pyroptosis as therapeutic targets for COVID-19. J Immunol 2020;205:307–12.
[10] Wei J, Shang R, Wang J, Zhu S, Yin J, Chen Y, et al. ACE2 overexpressing mesenchymal stem cells alleviates COVID-19 lung injury by inhibiting pyroptosis. Iscience 2022;25:1–19.
[11] Singh A, Strobbe D, Campanella M. Pyroptosis targeting via mitochondria: an educated guess to innovate COVID-19 therapies. Br J Pharmacol 2022;179:2081–5.
[12] Vora SM, Lieberman J, Wu H. Inflammasome activation at the crux of severe COVID-19. Nat Rev Immunol 2021;21:694–703.
[13] Cheng S-B, Nakashima A, Huber WJ, Davis S, Banerjee S, Huang Z, et al. Pyroptosis is a critical inflammatory pathway in the placenta from early onset preeclampsia and in human trophoblasts exposed to hypoxia and endoplasmic reticulum stressors. Cell Death Dis 2019;10:1–15.
[14] Hu JJ, Liu X, Xia S, Zhang Z, Zhang Y, Zhao J, et al. FDA-approved disulfiram inhibits pyroptosis by blocking gasdermin D pore formation. Nat Immunol 2020;21:736–45.
[15] Kerr JF, Wyllie AH, Currie AR. Apoptosis: a basic biological phenomenon with wide-ranging implications in tissue kinetics. Br J Cancer 1972;26:239–57.
[16] Wang TH, Wang HS. Apoptosis: (1) overview and clinical significance. J Formos Med Assoc 1999;98:381–93.
[17] Liu Z, Wang C, Yang J, Chen Y, Zhou B, Abbott DW, et al. Caspase-1 engages full-length gasdermin D through two distinct interfaces that mediate caspase recruitment and substrate cleavage. Immunity 2020;53. 106-14.e5.
[18] Tsuchiya K, Nakajima S, Hosojima S, Dinh Thi N, Hattori T, Thuong Manh L, et al. Caspase-1 initiates apoptosis in the absence of gasdermin D. Nat Commun 2019;10:1–19.
[19] Zheng ZD, Li GR. Mechanisms and therapeutic regulation of pyroptosis in inflammatory diseases and cancer. Int J Mol Sci 2020;21:1–16.

[20] Zhang P, Liu Y, Hu L, Huang K, Hong M, Wang Y, et al. NLRC4 inflammasome-dependent cell death occurs by a complementary series of three death pathways and determines lethality in mice. Sci Adv 2021;7:eabi9471.
[21] Li X, Zhang P, Yin Z, Xu F, Yang Z-H, Jin J, et al. Caspase-1 and Gasdermin D afford the optimal targets with distinct switching strategies in NLRP1b inflammasome-induced cell death. Research 2022;2022:1–17.
[22] Wang J. Perspectives on the landscape and flux theory for describing emergent behaviors of the biological systems. J Biol Phys 2022;48:1–36.
[23] Feng H, Zhang K, Wang J. Non-equilibrium transition state rate theory. Chem Sci 2014;5:3761–9.
[24] Fang XN, Kruse K, Lu T, Wang J. Nonequilibrium physics in biology. Rev Mod Phys 2019;91.
[25] Yan H, Zhang K, Wang J. Physical mechanism of mind changes and tradeoffs among speed, accuracy, and energy cost in brain decision making: landscape, flux, and path perspectives. Chin Phys B 2016;25:1–20.
[26] Wang J. Landscape and flux theory of non-equilibrium dynamical systems with application to biology. Adv Phys 2015;64:1–137.
[27] Li C, Wang J. Landscape and flux reveal a new global view and physical quantification of mammalian cell cycle. Proc Natl Acad Sci U S A 2014;111:14130–5.
[28] Chu X, Wang J. Microscopic chromosomal structural and dynamical origin of cell differentiation and reprogramming. Adv Sci 2020;7:1–15.
[29] Zhang K, Wang J. Exploring the underlying mechanisms of the coupling between cell differentiation and cell cycle. J Phys Chem B 2019;123:3490–8.
[30] Zhao L, Wang J. Uncovering the mechanisms of Caenorhabditis elegans ageing from global quantification of the underlying landscape. J R Soc Interface 2016;13:1–12.
[31] Yu C, Xu H, Wang J. A global and physical mechanism of gastric cancer formation and progression. J Theor Biol 2021;520:110643.
[32] Li C, Wang J. Quantifying the landscape for development and cancer from a core cancer stem cell circuit. Cancer Res 2015;75:2607–18.
[33] Wenbo L, Wang J. Uncovering the underlying mechanism of cancer tumorigenesis and development under an immune microenvironment from global quantification of the landscape. J R Soc Interface 2017;14:20170105.
[34] Yan H, Zhao L, Hu L, Wang X, Wang E, Wang J. Nonequilibrium landscape theory of neural networks. Proc Natl Acad Sci 2013;110. E4185-E94.
[35] Xu L, Zhang F, Zhang K, Wang E, Wang J. The potential and flux landscape theory of ecology. PLoS One 2014;9:1–17.
[36] Neher RA, Shraiman BI. Statistical genetics and evolution of quantitative traits. Rev Mod Phys 2011;83:1283.
[37] Van Valen L. 19. A New Evolutionary Law (1973). Foundations of Macroecology: University of Chicago Press; 2014. p. 284–314.
[38] Hu Y, Jiang Y, Li S, Ma X, Chen M, Yang R, et al. The Gasdermin D N-terminal fragment acts as a negative feedback system to inhibit inflammasome-mediated activation of Caspase-1/11. Proc Natl Acad Sci U S A 2022;119:e2210809119.
[39] Anderson MW, Moss JJ, Szalai R, Lane JD. Mathematical modeling highlights the complex role of AKT in TRAIL-induced apoptosis of colorectal carcinoma cells. Iscience 2019;12:182–93.
[40] Cheng X, Ferrell Jr JE. Apoptosis propagates through the cytoplasm as trigger waves. Science 2018;361:607–12.
[41] Bagci EZ, Vodovotz Y, Billiar TR, Ermentrout GB, Bahar I. Bistability in apoptosis: roles of Bax, Bcl-2, and mitochondrial permeability transition pores. Biophys J 2006;90:1546–59.
[42] Taabazuing CY, Okondo MC, Bachovchin DA. Pyroptosis and apoptosis pathways engage in bidirectional crosstalk in monocytes and macrophages. Cell Chem Biol 2017;24:507–14.
[43] Eling N, Morgan MD, Marioni JC. Challenges in measuring and understanding biological noise. Nat Rev Genet 2019;20:536–48.
[44] Engberg N, Kahn M, Petersen DR, Hansson M, Serup P. Retinoic acid synthesis promotes development of neural progenitors from mouse embryonic stem cells by suppressing endogenous, Wnt-dependent nodal signaling. Stem Cells 2010;28:1498–509.
[45] Wang J, Xu L, Wang E. Potential landscape and flux framework of nonequilibrium networks: robustness, dissipation, and coherence of biochemical oscillations. Proc Natl Acad Sci 2008;105:12271–6.
[46] Lang JT, Nie Q, Li CH. Landscape and kinetic path quantify critical transitions in epithelial-mesenchymal transition. Biophys J 2021;120:4484–500.
[47] Xu F, Li X, Wu R, Qi H, Jin J, Liu Z, et al. Topological design principle for the robustness of necroptosis biphasic, emergent, and coexistent (BEC) dynamics. bioRxiv 2023;23:525173.
[48] Wells DK, Kath WL, Motter AE. Control of stochastic and induced switching in biophysical networks. Phys Rev X 2015;5:031036.
[49] Zhou X, Ren W. Adaptive minimum action method for the study of rare events. J Chem Phys 2008;128:1–12.
[50] Wang J, Zhang K, Xu L, Wang E. Quantifying the Waddington landscape and biological paths for development and differentiation. Proc Natl Acad Sci U S A 2011;108:8257–62.
[51] Wang J, Zhang K, Wang E. Kinetic paths, time scale, and underlying landscapes: a path integral framework to study global natures of nonequilibrium systems and networks. J Chem Phys 2010;133:125103.
[52] Qiu K, Gao K-f, Yang L-j, Zhang Z-k, Wang R, Ma H-s, et al. A kinetic model of multiple phenotypic states for breast cancer cells. Sci Rep 2017;7:1–13.
[53] He P, Qiu K, Jia Y. Modeling of mesenchymal hybrid epithelial state and phenotypic transitions in EMT and MET processes of cancer cells. Sci Rep 2018;8:1–11.
[54] Ye L, Li C. Quantifying the landscape of decision making from spiking neural networks. Front Comput Neurosci 2021;15:1–18.
[55] Yin Z, Zhang PP, Xu F, Liu Z, Zhu L, Jin J, et al. Cell death modes are specified by the crosstalk dynamics within pyroptotic and apoptotic signaling. Chaos 2021;31:093103.
[56] Frauenfelder H, Parak F, Young RD. Conformational substates in proteins. Annu Rev Biophys Biophys Chem 1988;17:451–79.
[57] Frauenfelder H, Sligar SG, Wolynes PG. The energy landscapes and motions of proteins. Science 1991;254:1598–603.
[58] Austin RH, Beeson K, Eisenstein L, Frauenfelder H, Gunsalus I. Dynamics of ligand binding to myoglobin. Biochemistry 1975;14:5355–73.
[59] Wang J, Oliveira RJ, Chu X, Whitford PC, Chahine J, Han W, et al. Topography of funneled landscapes determines the thermodynamics and kinetics of protein folding. Proc Natl Acad Sci 2012;109:15763–8.
[60] Zheng X, Liu Z, Li D, Wang E, Wang J. Rational drug design: the search for Ras protein hydrolysis intermediate conformation inhibitors with both affinity and specificity. Curr Pharm Des 2013;19:2246–58.
[61] Chu X, Liu F, Maxwell BA, Wang Y, Suo Z, Wang H, et al. Dynamic conformational change regulates the protein-DNA recognition: an investigation on binding of a Y-family polymerase to its target DNA. PLoS Comput Biol 2014;10:e1003804.
[62] Wang Y, Chu X, Longhi S, Roche P, Han W, Wang E, et al. Multiscaled exploration of coupled folding and binding of an intrinsically disordered molecular recognition element in measles virus nucleoprotein. Proc Natl Acad Sci 2013;110. E3743-E52.
[63] Liu F, Chu X, Lu HP, Wang J. Molecular mechanism of multispecific recognition of calmodulin through conformational changes. Proc Natl Acad Sci 2017;114. E3927-E34.
[64] Yan Z, Wang J. Optimizing the affinity and specificity of ligand binding with the inclusion of solvation effect. Proteins: Struct, Funct, Bioinf 2015;83:1632–42.
[65] Yan Z, Wang J. Optimizing scoring function of protein-nucleic acid interactions with both affinity and specificity. PLoS One 2013;8:e74443.
[66] Yan Z, Guo L, Hu L, Wang J. Specificity and affinity quantification of protein–protein interactions. Bioinformatics 2013;29:1127–33.
[67] Yan Z, Wang J. Funneled energy landscape unifies principles of protein binding and evolution. Proc Natl Acad Sci 2020;117:27218–23.
[68] Yan Z, Wang J. Superfunneled energy landscape of protein evolution unifies the principles of protein evolution, folding, and design. Phys Rev Lett 2019;122:018103.
[69] Zhu L, Li X, Xu F, Yin Z, Jin J, Liu Z, et al. Network modeling-based identification of the switching targets between pyroptosis and secondary pyroptosis. Chaos, Solitons Fractals 2022;155:1–12.
[70] Li X, Zhong C-Q, Wu R, Xu X, Yang Z-H, Cai S, et al. RIP1-dependent linear and nonlinear recruitments of caspase-8 and RIP3 respectively to necrosome specify distinct cell death outcomes. Protein Cell 2021;12:858–76.